Morphologic three-dimensional scanning of fallopian tubes to assist ovarian cancer diagnosis

Wendy-Julie Madore
Etienne De Montigny
Andréanne Deschênes
Fouzi Benboujja
Mikaël Leduc
Anne-Marie Mes-Masson
Diane M. Provencher
Kurosh Rahimi
Caroline Boudoux
Nicolas Godbout

Morphologic three-dimensional scanning of fallopian tubes to assist ovarian cancer diagnosis

Wendy-Julie Madore,[a,b,c] Etienne De Montigny,[a,b] Andréanne Deschênes,[a] Fouzi Benboujja,[a] Mikaël Leduc,[a] Anne-Marie Mes-Masson,[b,c,d] Diane M. Provencher,[b,c,e] Kurosh Rahimi,[b,c] Caroline Boudoux,[a] and Nicolas Godbout[a,*]

[a]École Polytechnique Montréal, Centre d'Optique, Photonique et Lasers (COPL), Montreal, Canada
[b]Centre de recherche du Centre hospitalier de l'Université (CRCHUM), Cancer and Imaging and Engineering Departments, Montreal, Canada
[c]Institut du cancer de Montréal, Montreal, Canada
[d]Université de Montréal, Department of Medicine, Montreal, Canada
[e]Université de Montréal, Division of Gynecologic Oncology, Montreal, Canada

Abstract. The majority of high-grade serous ovarian cancers is now believed to originate in the fallopian tubes. Therefore, current practices include the pathological examination of excised fallopian tubes. Detection of tumors in the fallopian tubes using current clinical approaches remains difficult but is of critical importance to achieve accurate staging and diagnosis. Here, we present an intraoperative imaging system for the detection of human fallopian tube lesions. The system is based on optical coherence tomography (OCT) to access subepithelial tissue architecture. To demonstrate that OCT could identify lesions, we analyzed 180 OCT volumes taken from five different ovarian lesions and from healthy fallopian tubes, and compared them to standard pathological review. We demonstrated that qualitative features could be matched to pathological conditions. We then determined the feasibility of intraluminal imaging of intact human fallopian tubes by building a dedicated endoscopic single-fiber OCT probe to access the mucosal layer inside freshly excised specimens from five patients undergoing prophylactic surgeries. The probe insertion into the lumen acquired images over the entire length of the tubes without damaging the mucosa, providing the first OCT images of intact human fallopian tubes. © 2017 Society of Photo-Optical Instrumentation Engineers (SPIE) [DOI: 10.1117/1.JBO.22.7.076012]

Keywords: optical coherence tomography; ovarian cancer; fallopian tubes; single-fiber probe.

Paper 170187R received Mar. 24, 2017; accepted for publication Jun. 29, 2017; published online Jul. 20, 2017.

1 Introduction

Ovarian cancer is the fifth leading cause of cancer deaths[1] in women and the most lethal gynecological malignancy, with a 5-year survival rate of only 40%.[2] Because the disease is primarily asymptomatic at early stages or associated with nonspecific symptoms, the majority of ovarian cancers is diagnosed at a late stage when the disease has already spread within the peritoneal cavity and curative strategies are largely ineffective.[3,4] Screening methods, such as transvaginal ultrasound (US) and blood levels of biomarker CA125, have been ineffective with little impact in reducing mortality and have, instead, generated greater distress and risk of unnecessary surgery.[3,5] Consequently, both the US Preventive Services Task Force and the American College of Obstetricians and Gynecologists do not recommend routine screening for ovarian cancer in the general population or among asymptomatic women, and there is insufficient evidence to implement routine screening for women who carry genetic mutations that place them at high risk.[5,6] Women in the general population have a 1% to 2% life risk of developing ovarian cancer, whereas women with familial history or with mutations in the homologous recombination DNA repair genes BRCA1 and BRCA2 have a significantly higher predisposition to ovarian cancer. Women carrying BRCA1 and BRCA2 mutations face a lifetime risk of 50% and 20%, respectively.[5] However,

when detected at an early stage, localized ovarian cancer has a much improved 5-year survival rate that is >90%.[3,5] For high-risk women, it is especially crucial to develop effective screening strategies for early detection and prevention of advanced disease.

The standard of care for advanced ovarian cancer involves cytoreductive (debulking) surgery with the goal of removing or reducing tumor burden.[7] Alternatively, women may receive neoadjuvant chemotherapy followed by interval debulking surgery, particularly if they have advanced disease or are not fit for primary surgery.[7,8] Prophylactic surgeries, which include the removal of fallopian tubes and/or ovaries, are practiced as a prevention strategy in women at high risk as studies have demonstrated a drastic reduction in the risk of ovarian, fallopian tube, and peritoneal cancers for women carrying BRCA mutations.[3,9,10] Following surgery, a pathologist performs a thorough macroscopic and microscopic examination of the excised tissues. Even the most stringent histopathologic protocol (sectioning and extensively examining the fimbriated end) only samples 0.5% of the fallopian tubes. In this context, submillimeter pathologies can remain undetected. Moreover, surgical procedures and management can vary across hospitals, and the careful dissection of the entire length of the fallopian tube is not universally conducted. Imaging tools to guide histopathologic examination could reduce the risk of undetected suspicious or cancerous lesions. Imaging procedures have also been used

*Address all correspondence to: Nicolas Godbout, E-mail: nicolas.godbout@polymtl.ca

to examine disease burden and include US, computed tomography, positron emission tomography, and magnetic resonance imaging. Although these techniques allow for deep tissue visualization, the resolution of these techniques is not suited for the early detection of small tumors and lesions,[2,11] both at the screening and diagnostic levels.

At the molecular and histological level, ovarian cancer is a heterogeneous disease and is clinically diverse, with the majority of cases classified as epithelial ovarian cancer (EOC). There are five main subtypes of EOC that differ in cell origins, pathogenesis, and pathology: mucinous, endometrioid, clear cell, low-grade serous (LGS), and high-grade serous (HGS).[3] HGS ovarian cancer is the most common and most lethal subtype of EOCs.[3] Although the ovarian surface epithelium was historically believed to be the etiological site for HGS carcinomas, evidence now indicates that precursor lesions originate in the fallopian tubes as serous tubal intraepithelial carcinomas (STICs).[3,5] While a significant proportion of HGS ovarian cancers arise from STIC lesions that develop in fallopian tubes, these lesions measure only a few hundred micrometers, escaping detection even on rigorous pathological evaluations. HGS ovarian tumors arise from the proximal end of the fallopian tubes, spread to the ovaries, and, in more advanced disease, metastasize to the abdominal cavity.[12,13] A dedicated detection instrument must consider the specific characteristics of ovarian cancer, such as the large area covered by the organs of interest (fallopian tubes and ovaries), the heterogeneity of the tumors, and the high metastatic potential of epithelial lesions. There is a critical need for an efficient tool allowing for internal visualization of suspicious lesions or morphological changes that indicate early stage of disease in the fallopian tube.

Optical imaging techniques are good candidates to address these requirements. They can be implemented through endoscopic probes small enough to be inserted inside the uterus and fallopian tubes. They also allow for fast imaging, with the ability to perform optical biopsies without damaging the tissue. Among morphological imaging techniques, confocal imaging has been used to image ovaries *in vivo*[14–16] and in fallopian tubes[17] using contrast agents such as acridine orange. Multiphoton imaging, which does not require a contrast agent, has been used on ovaries to find optical biomarkers.[18,19] On the other hand, molecular imaging techniques can provide more specific information, regardless of tissue structure. Fluorescence imaging of ovaries and fallopian tubes has been used intraoperatively using fluorescein-binded folate-alpha.[20] *Ex vivo* fluorescence imaging was also performed using the natural autofluorescence of ovaries[21–23] and fallopian tubes.[24,25] Raman spectroscopy is another molecular imaging technique that can distinguish normal from malignant ovaries.[26,27]

Optical coherence tomography (OCT) is a laser-based interferometric technique that allows for transverse visualization of tissue without any fixation, slicing, or staining.[28] This imaging technique identifies morphological features of the sample and can yield qualitative and quantitative information on tissue architecture. State-of-the-art OCT implementation allows for fast imaging speed[29,30] and is robust enough for use in clinical settings.[30–33] OCT is now performed as a routine clinical evaluation of the retina in ophthalmology[33–35] and has been used for Barrett's oesophagus detection in gastroenterology[31,36,37] and in cardiology applications for vulnerable plaque detection.[38,39]

OCT has also been used in gynecology for specific applications, such as *in vivo* inspection of the cervix[40] and endometrial tissue in both *ex vivo*[40,41] and *in vivo* studies.[42] Ovaries and fallopian tubes have also been investigated *in vitro* using bench-top systems.[43,44] A laparoscopic OCT probe was built to assess *in vivo* the condition of the isthmus, the smallest part of the fallopian tube,[45] and ovaries.[46,47] The design and the validation of an endoscopic OCT probe is primarily application driven. Recently, a promising flexible probe for fallopian tube imaging has been demonstrated, combining OCT with reflectance imaging.[48] Scanning mechanisms can also be included into the imaging probe to enhance the field of view including rotary junctions,[37,49] mounted mirrors,[30,46] and motorized pullback.[46,48,50] The design of very small probes (outside diameter of 1 mm or less) has been demonstrated in some of these implementations.[30,48,51]

Recent progress in optical imaging, as previously highlighted, can be beneficial to ovarian cancer screening and diagnostics. Rigorous inspection of fallopian tubes with an instrument capable of identifying submillimeter suspicious lesions can effectively reduce the burden of extensive histopathologic examination protocols. In a long-term perspective, a similar tool could be envisioned for direct *in vivo* screening, adding flexibility to management of high-risk patients.

In this study, we investigate the potential of OCT as a morphological imaging technique for qualitative and exhaustive analysis of the mucosal layer of fallopian tubes for diagnostic purposes. Using a bench-top OCT system, we present a preliminary comparison of OCT images of human ovaries and fallopian tubes with corresponding histology. We analyze the five most frequent subtypes of ovarian cancer, which may involve the fallopian tube at some point in the cancer's progression. We also investigate the potential of OCT for intraluminal imaging of human fallopian tubes. The OCT system was coupled to an all-fiber endoscopic probe, specifically designed for direct insertion into the fallopian tube and was capable of imaging epithelial and subepithelial structures over 10 cm in length. We present the design as well as the optical and mechanical characterization of this probe and demonstrate its application for OCT imaging of intact, freshly excised human fallopian tubes from five patients.

2 Methodology

2.1 Optical Coherence Tomography System

The OCT system (Fig. 1) is a wavelength-swept micro-electro-mechanical system vertical-cavity surface-emitting laser (MEMS VCSEL; Thorlabs, New Jersey) centered at 1300 nm and coupled to an interferometer and a data acquisition module (500 MS/s; ATS9350, Alazar Technologies, Canada). The swept-source has an average output power of 35 mW with an A-line scan rate at 100 kHz. The first of two configurations [Fig. 1(a)] involved a conventional bench-top commercial version, using a Michelson interferometer and a bulk imaging head. The scan lens is an LSM03 5× objective (Thorlabs, New Jersey), with an effective focal length of 36 mm. The imaging head of the bench-top configuration yields a lateral resolution of 25 μm and depth resolution of 15 μm in air. The field of view covers a volume of 10 mm × 10 mm × 5 mm. Data acquisition of a volume takes 17 s (10 mm × 10 mm × 5 mm, 1024 × 1024 × 512 voxels). The second configuration [Fig. 1(b)] uses the same laser and data acquisition module but uses an endoscopic probe in a common-path interferometer with an AC-coupled dual-balanced detector
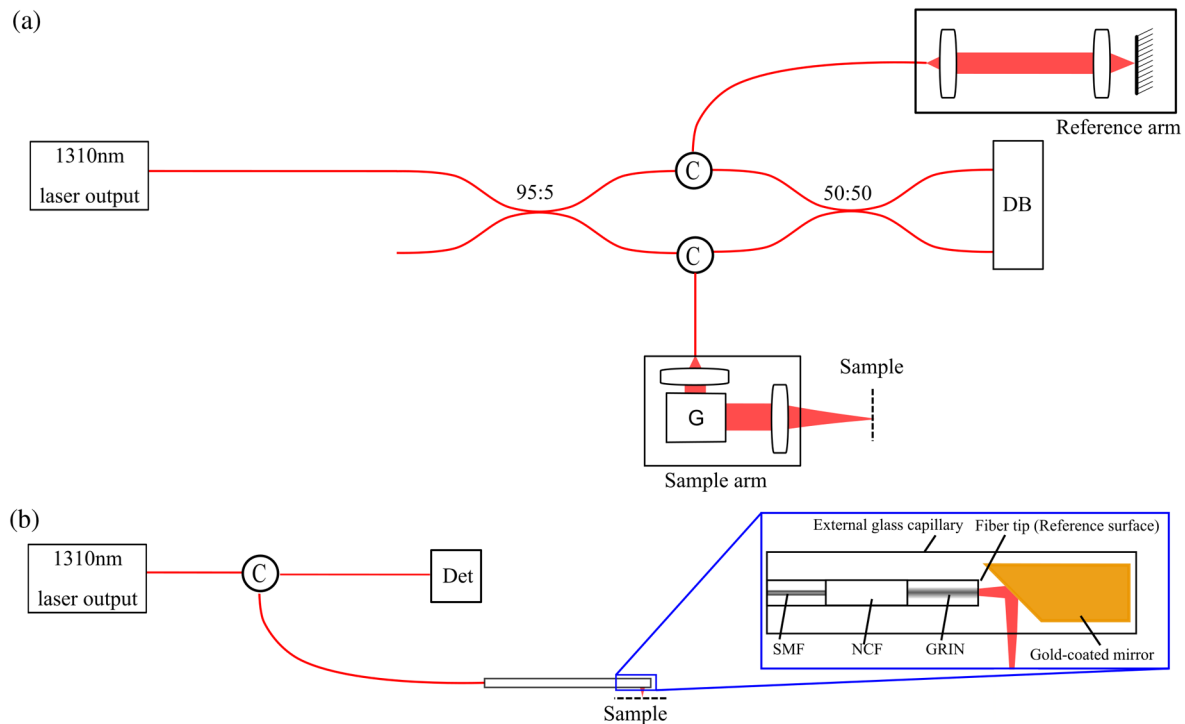
Fig. 1 System configurations for the acquisition of fallopian and ovarian tissue images. Schematic diagram of the commercial bench-top version is presented in (a), with the addition of a custom external reference arm. The probe configuration is presented in (b). The probe images using common-path interferometry, using the fiber tip as the reference surface. Additional details on the construction of the probe are presented in Fig. 4. C, circulator; G, galvanometer-mounted mirror; DB, dual-balanced detector; Det, AC-coupled detector; SMF, single-mode fiber; NCF, no core fiber; and GRIN, graded-index fiber.

(PDB410C-AC, Thorlabs, New Jersey). The probe yields resolutions of 23 μm × 25 μm × 15 μm ($x \times y \times z$).

2.2 Patient Samples

Formalin-fixed paraffin-embedded (FFPE) samples and freshly excised tissues were from women who underwent surgeries at the Centre hospitalier de l'Université de Montréal (CHUM). All patients provided written informed consent. FFPE samples were from the tissue bank protocol #BD04.002, whereas fresh tissues were collected using protocol #14.159, both of which were approved by the research ethics board of the CHUM. This proof-of-principle relies on FFPE samples to test OCT contrast, as the tissue bank offers a wide array of cancer subtypes collected throughout the years. Some subtypes have a very low occurrence in patients, the most efficient and cost-effective way to analyze these pathology specimens was through the tissue bank. FFPE samples were selected based on the associated pathology report. A total of 52 FFPE blocks, each from a different patient, were selected among six categories: HGS tumors (12), healthy fallopian tubes (12), endometrioid tumors (7), mucinous tumors (7), LGS tumors (7), and clear cell tumors (7). Each block was installed on the bench-top OCT system and scanned to extract tissue features within an area of 10 mm × 10 mm with a depth of 5 mm. Depending on the specimen, 3 to 5 scans were required to cover the entire sample surface. All scans were taken with a small overlap facilitating the registration process and allowed for a virtual reconstruction of all features. For each paraffin block, a hematoxylin and eosin (H&E)-stained slide was obtained for comparison.

2.3 Intraluminal Imaging

An all-fiber endoscopic probe was developed to meet the stringent requirements for imaging inside human fallopian tubes. The custom probe was designed and built to be resistant enough to withstand insertion in biological samples while preserving an outside diameter close to 1 mm. Focusing optics were integrated at the optical fiber tip to increase robustness and compactness. The fiber probe design was validated and assembled based on the specifications obtained from optical simulations (OSLO, Lambda Research, Massachusetts). The probe optical characteristics obtained from the simulations were then measured and compared to the previous images acquired on animal models[52] and *ex vivo* human fallopian tubes. In agreement with CHUM protocol #14.159, imaging was performed on five patients undergoing a complete hysterectomy with bilateral salpingo-oophorectomy next to the operating room theater. Samples then underwent pathological examination to establish a definitive diagnosis.

3 Results

3.1 Paraffin-Embedded Specimen Imaging

In the bench-top OCT configuration, six types of specimens representing EOC pathologies and normal tissue were selected and imaged. A total of 52 samples were scanned resulting in 180 OCT volumes. Representative *en face* images with corresponding histology are shown in Fig. 1 with a single image presented per type of pathology. Figures 2(a) and 2(b) show transverse images of a healthy fallopian tube by OCT and histology (H&E staining), which revealed multiple structures such as
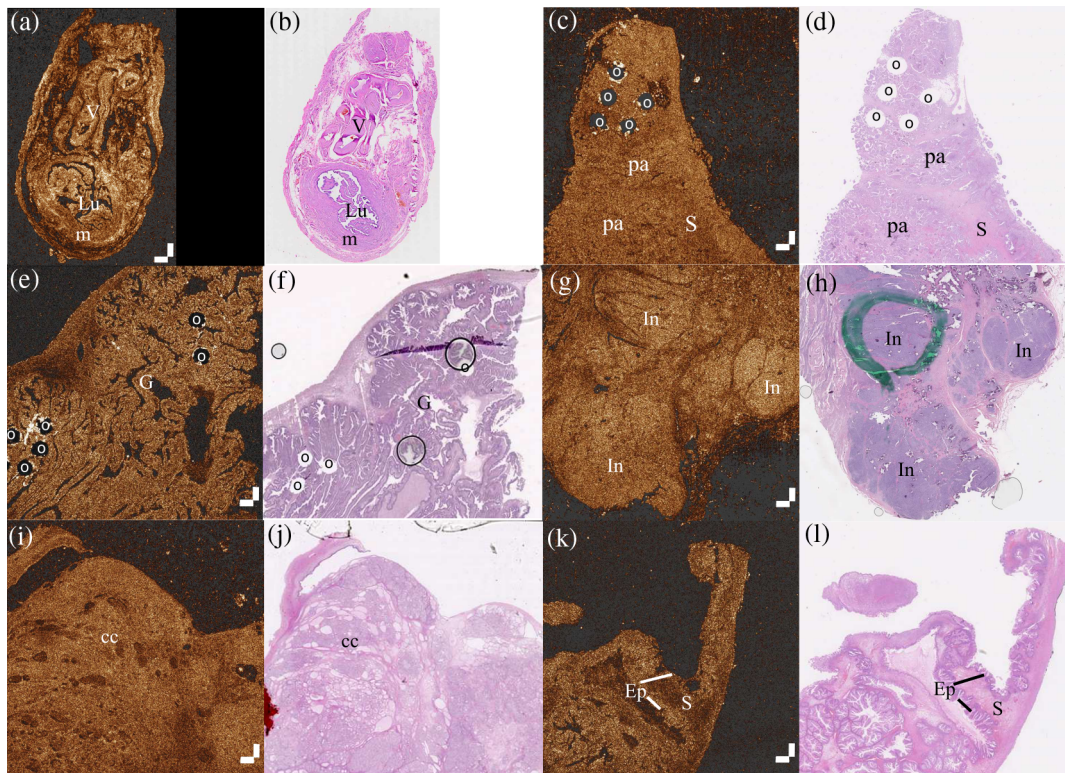
Fig. 2 *En face* OCT images of paraffin-embedded human EOCs or normal specimens paired with the corresponding histology (H&E) section. All OCT images are represented by (a, c, e, g, i, and k). All H&E sections are represented by (b, d, f, h, j, and l). (a) and (b) show healthy fallopian tube in transverse sections, (c) and (d) show LGS tumor, (e) and (f) show endometrioid tumor, (g) and (h) show HGS tumor, (i) and (j) show clear cell tumor, and (k) and (l) show mucinous tumor. Punch holes in the tissue are marked with a circle (o). Lu, lumen; m, muscle layer; V, blood vessels; pa, papillary architecture; S, stroma; G, glandular structure; In, stromal invasion; cc, clear cells; and Ep, epithelium. All OCT images are 10 mm × 10 mm and scale bars are 500 μm.

the tubal lumen (Lu) and the surrounding muscle wall (M), as well as a cluster of blood vessels (V) outside the fallopian tube. Figure 2(c) shows an OCT cross-sectional image of an LGS tumor with corresponding histology [Fig. 2(d)], and demonstrated stroma (S) in distinct contrast to regions of papillary architecture (PA). Pathology of an endometrioid tumor was confirmed by OCT and histology [Figs. 2(e) and 2(f)] showing that the sample was mainly constituted of glandular growth (G), very similar to glandular endometrial tumors. For an HGS tumor, both OCT and histology [Figs. 2(g) and 2(h)] showed a carcinoma with solid architecture, which appeared dense in comparison to the stroma due to the higher number of nuclei (purple regions in the histology translated into brighter regions on OCT). In opposition, the histological section of a clear cell tumor shown in Fig. 2(j) had unstained cytoplasm (CC) and presented a tubulo-cystic architecture, whereas the corresponding OCT section [Fig. 2(i)] appeared more heterogeneous. Finally, Figs. 2(k) and 2(l) present the OCT image and histology, respectively, of a part of a mucinous tumor and show that the stratified columnar epithelium (Ep) lining was distinct from the ovarian stroma (S).

Our macroscopic comparisons showed good structural agreement between the histology and OCT images. We then examined samples on a microscopic level to determine if relevant diagnostic information could be identified. *En face* OCT images of HGS and LGS cancer samples at 5× magnification are shown in Figs. 3(a) and 3(e), respectively, whereas corresponding

histological sections are shown in Figs. 3(d) and 3(h). Insets represent 10× magnifications of each tumor. Since the lateral resolution of the bench-top system was 25 μm, details smaller than this limit were not visible. Carcinoma with solid architecture was revealed in the HGS tumor and marked with an asterisk (*), whereas PA was evident in the LGS tumor, marked with a cross (†). Healthy stroma, as indicated by arrows, appeared slightly darker than cancerous tissue.

3.2 Custom-Built Optical Coherence Tomography Probe for Intraluminal Imaging

To examine the potential of OCT for intraluminal imaging of freshly excised human fallopian tubes, we designed a custom-built imaging probe to use as a replacement of the bulk scanning head of the OCT system previously described. To withstand insertion into the fallopian tube without assistance of an outer canule, the probe was designed as a rigid cylinder of 10 cm in length. The probe wall consisted of hard glass tubing and the tip was capped with optical glue to prevent perforation and minimize tissue trauma during insertion. Within the glass tubing, the optical fiber was covered with a protective hytrel jacket (extending to the fiber connection) to prevent mechanical damage during manipulation. Figure 4 presents the main features and characteristics of this endoscopic probe. The final outer diameter was 1.2 mm and allowed for both contact and noncontact imaging.
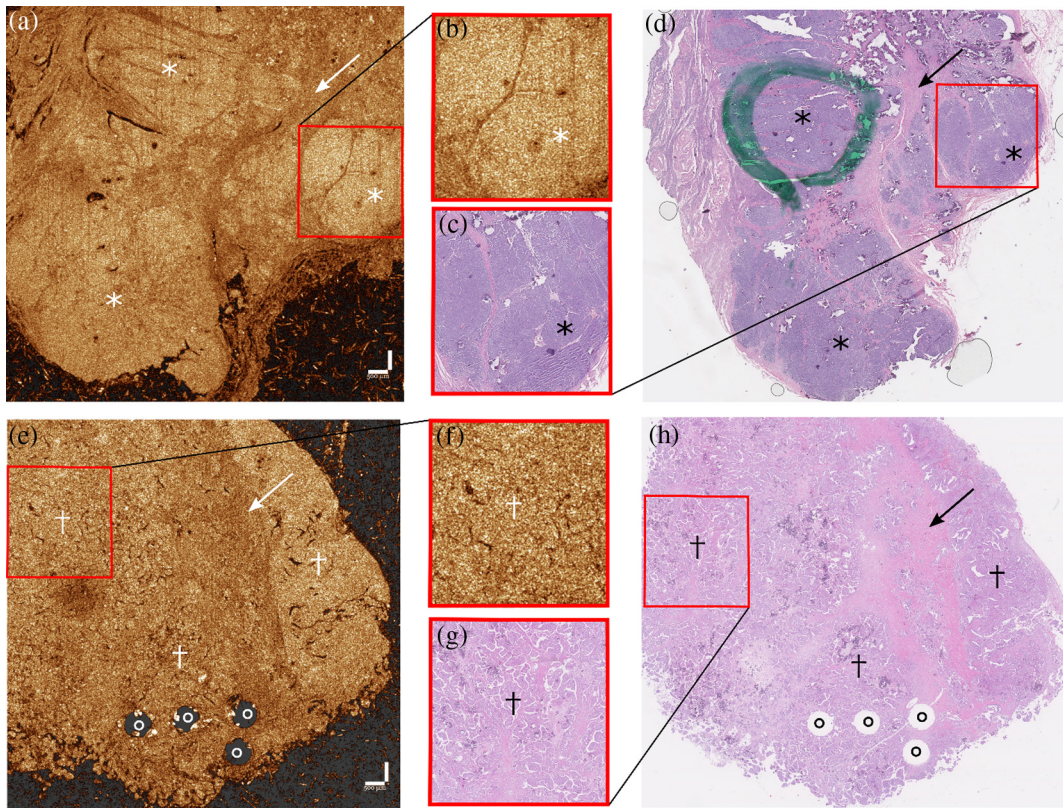
Fig. 3 *En face* OCT images of HGS and LGS ovarian tumors at 5× magnification (a, e) and 10× magnification (b, f) with the corresponding histology (H&E). (a) OCT segment of HGS ovarian tumor with magnification of a cancerous region (b). The histology slice is shown in (d) with magnification (c), corresponding to (a) and (b), respectively. This type of tumor has carcinomas with solid architecture (*) around the stroma (arrow). (e) OCT segment of an LGS ovarian tumor with an enlargement of the cancerous zone shown in (f). The corresponding histology and magnification are shown, respectively, in (h) and (g). LGS tumors present a PA (crosses) around the stroma (arrow). Holes (circles o) represent sections punctured from the sample for external analyses. Scale bar: 500 μm.

All the focusing optics were directly implemented into the optical fiber. The probe consisted of 2 m of SMF-28 fiber (Corning, New York), a spacer of no core fiber (NCF, custom-drawn pure silica fiber, COPL, Laval University, Canada), and a graded-index fiber (GRIN—GIF625, Thorlabs, New Jersey). The SMF-28 has a core of 8.2 μm, an outer diameter of 125 μm and a numerical aperture (NA) of 0.12. The NCF is a highly multimode fiber with a guiding coating jacket with a diameter of 125 μm and a 0.5 NA. The GRIN fiber is a graded-index and bend-tolerant multimode fiber with an inner cladding of 62.5 μm, an outer cladding of 125 μm, and a 0.275 NA. The length of the spacer (180 μm) and the GRIN (300 μm) were selected through simulations to provide optimal imaging at a focal distance of 2 mm away from the outside wall of the probe with a simulated diffraction limit of <60 μm over the imaging range of 2 mm. To provide a side view, an angled-polished rod mirror (#47-628, Edmund Optics, New Jersey) was mounted at the tip of the probe within the glass tubing. A gold coating was applied to the mirrors to increase the reflectivity. The coating was a three-layer structure of high reflectivity and of high surface quality that is composed of 30 nm of chromium, 200 nm of gold, and a protective layer of 20 nm of pure silica. With this modification, the probe's transmission of near infrared light (1250 to 1350 nm) was improved from 65% to 95%.

Figure 5 presents simulations of the main optical characteristics of the probe using optics software for layout and optimization (OSLO, Lambda Research, Massachusetts). The spot diagram [Fig. 5(a)] of the output beam was computed for five distances away from the output window, ranging from 0 to 2 mm away from the probe's external wall, at 0.5 mm increments. An Airy disk of 43 μm, drawn in black on each sketch, shows that all the paraxial rays are included within the diffraction limit. Figure 5(b) represents the simulated point spread function for each axis and shows a relatively small presence of astigmatism. Coddington sags factors obtained from the simulations indicated a nearly collimated beam in both axes (x, y), with a residual focal length of −37 mm in the *x*-plane and −2 mm in the *y*-plane. The schematic diagram of the simulation is shown in Fig. 5(c) and represents the beam propagation (*z*-axis) corresponding to the imaging direction (A-line). The probe has an effective focal length of 256 μm and an NA of 0.024. The chromatic focal shift over the spectrum of the OCT source is 10 μm between 1250 and 1350 nm. The inset shows an image of a human finger acquired with the probe.

The three-fibered parts of the probe were sequentially spliced together using a filament fusion splicing system (FFS-2000, Vytran Corporation, New Jersey). Each piece of NCF and GRIN was carefully spliced and cleaved to the right length, then measured and inspected with the splicer's visualization
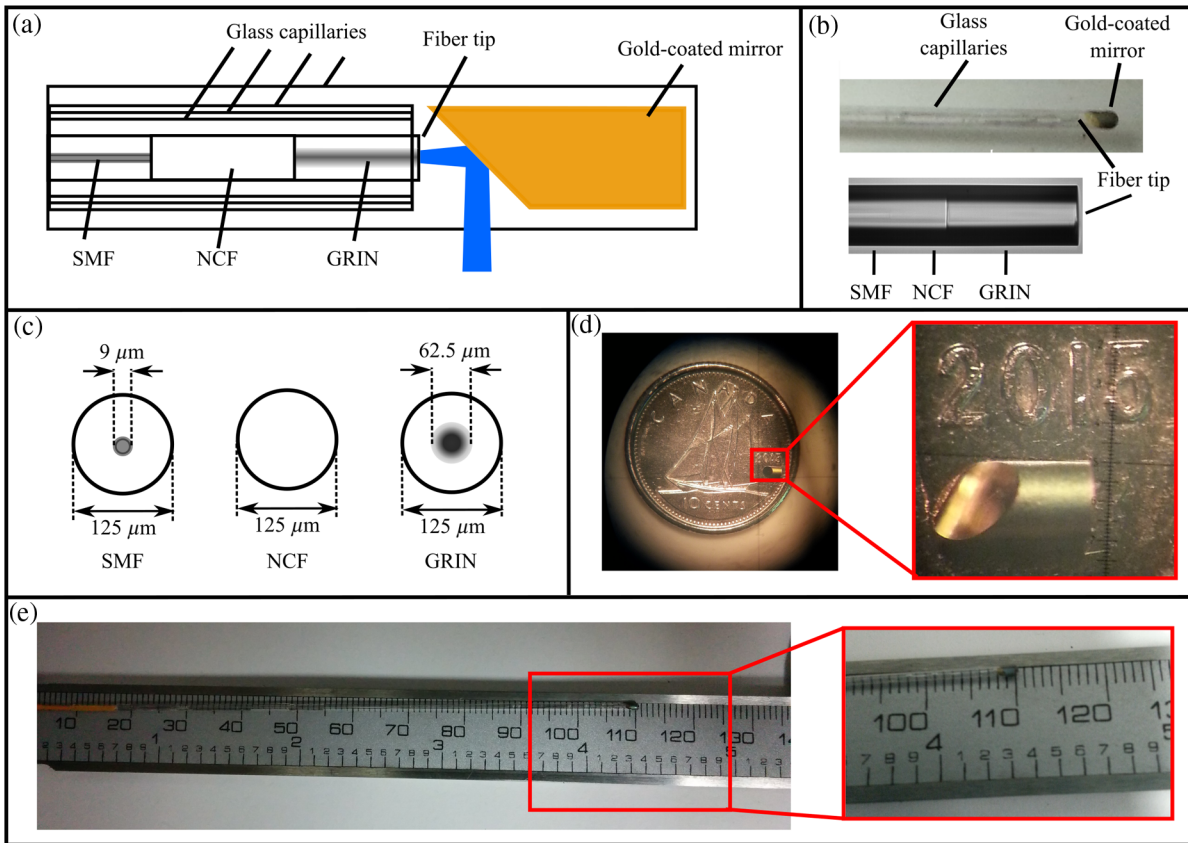
Fig. 4 Descriptive diagrams and photographs of the probe. (a) Schematic diagram of the assembly in the tip. (b) Photographs of the complete probe. (c) Dimensions of the three fibers used as focusing optics. (d) Photograph and a magnified view of the gold-coated mirror with a Canadian dime for size comparison. (e) Full length of the rigid part of the probe with an inset showing a closer view of the tip.
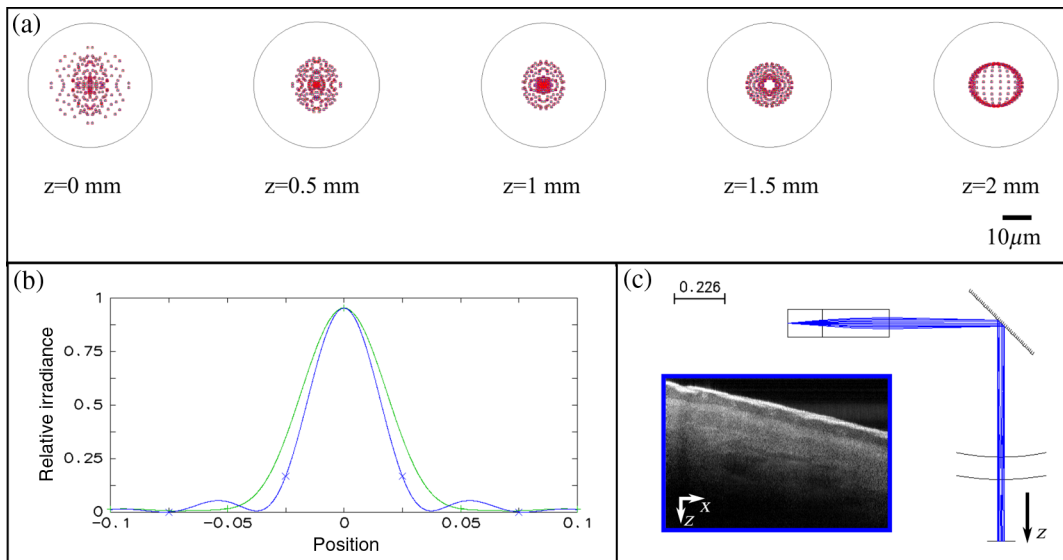

Fig. 5 Optical specifications of the probe. (a) Spot diagram computed with OSLO for five distances from the probe's outer surface to 2 mm away from the probe. (b) Point spread function of the beam in the *x* and *y* planes at the plane of best focus. (c) 2-D layout of the simulated probe, as well as the coordinate system. A-lines are acquired in the *z* direction and the inset outlined in the blue box presents an image of a human finger acquired with the probe. For (b) and (c), units are in mm.

camera. This part of the probe was then inserted into three clean, clear fused quartz capillaries (#CV2033, CV4055, and CV6084, VitroCom, New Jersey) that were held together with optical glue. This encapsulated fiber probe was inserted into the clean, clear fused quartz capillary (#CV1012, VitroCom, New Jersey) and placed close to the gold-coated mirror at the tip of the final assembly. When an optimal placement of the fiber tip and the mirror was reached, components were glued together with optical glue. The tip of the probe was rounded off and polished to minimize tissue damage during insertion. A protective 900 μm hytrel jacket was added on the fiber outside the tubing for additional mechanical protection.

After assembly, the probe was optically characterized to ensure its performance met the design specifications. Measured lateral resolutions were 23 and 25 μm in x and y planes, respectively. These values corresponded to edge responses acquired using a USAF1951 resolution target and compared well with the simulated resolutions in air of 22 and 26 μm, respectively. Axial resolution (z) was 15 μm in air. Imaging depth in diffusive soft tissue samples, such as human finger and uterus, was ∼2 mm.

3.3 Imaging of Freshly Excised Fallopian Tubes

Reproductive tissues and specimens were obtained from five patients undergoing prophylactic surgery and were imaged within 30 min before pathological examination. Human fallopian tubes were imaged using the custom endoscopic probe. Images of uteri, ovaries, and fallopian tubes were also acquired using the bench-top configuration. All imaging sessions included a macroscopic examination of the sample. The bench top was then used to image the exterior part of the fimbriated ends of the tube. The probe was inserted into one fallopian tube from the proximal end (close to the ovary) toward the uterus. Complete insertion time ranged from 20 s to 1 min, depending on the tube's condition and length. Probe insertion up to the isthmic part in both fallopian tubes was successful in all five patients' samples. After insertion, a pullback was performed to acquire a 2-D image over the entire length of the tube. The process was then repeated at other angles to collect four scans per fallopian tube. The last centimeter of the isthmus and uterotubal junction was not acquired due to size constraints. Regions of interest were marked with small surgical tacks in the peritoneum surrounding the tubes for pathological examination.

Photographs and images of a freshly excised specimen with fallopian tubes and probe insertion are presented in Fig. 6. A transverse histology of the fallopian tube after four insertions is presented in Fig. 6(d) with the insertion site noted by the (*) as in Figs. 6(a) and 6(b). An OCT image of a pullback covering 10 cm in length is presented in Fig. 6(e) with magnifications of the ampulla and fimbriated end of the tube [Figs. 6(f) and 6(g)]. The mucosal layer of the fallopian tubes (L), in contact with the probe, appears in the center region of Fig. 6(e). The peritoneum (P) and muscle (M) form the external layers of
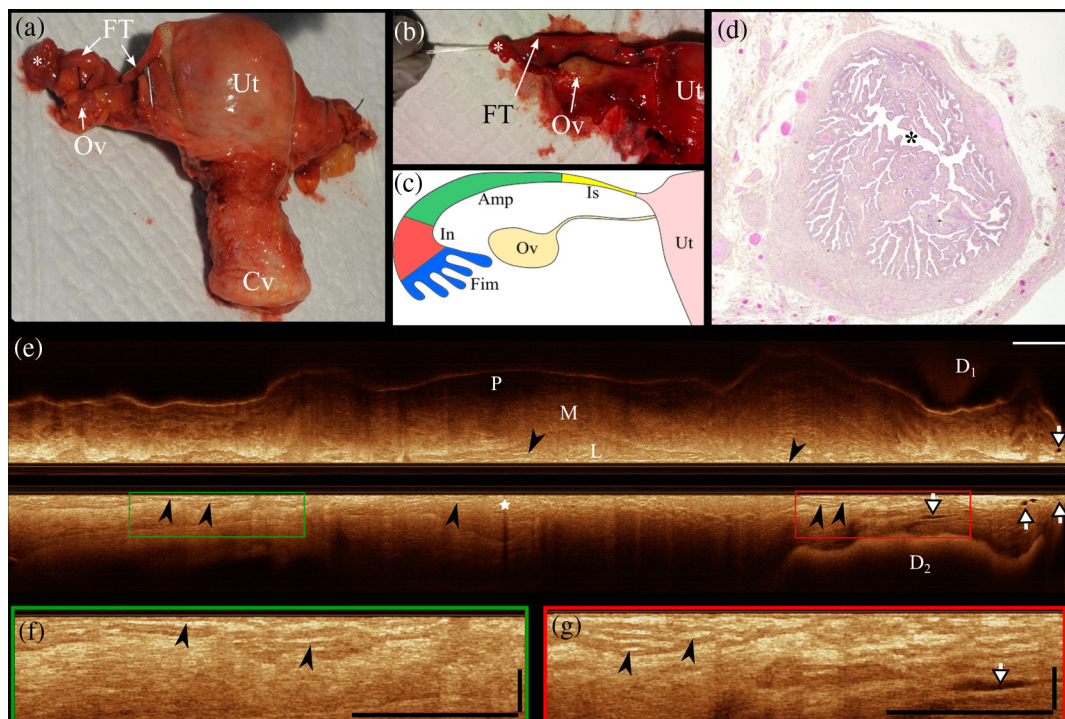

Fig. 6 OCT pullback of a freshly excised human fallopian tube. (a) Photograph of the patient's specimen and (b) photograph taken during insertion of the probe in the fallopian tube. (c) Drawing of corresponding fallopian tube illustrating the isthmus (Is), ampulla (Amp), infundibulum (In), and fimbriated end (Fim). (d) H&E slide of the tube in the region of the infundibulum. Repeated probe insertion at the site identified by (*) on images (a), (b), and (d) did not create damage. (e) Pullback on a length of 10 cm. Magnifications of OCT pullback show the ampulla (f) as well as infundibulum and fimbriated end (g), both of which are highlighted in green and red boxes, respectively, in (e). Layers of microvilli are pointed by the black arrowheads. White arrows point to edema regions, which differ from blood vessels (white star). FT, Fallopian tube; Ov, ovary; Ut, uterus; Cv, cervix; Lu, lumen; M, muscle; P, peritoneum; and D, finger. Scale bars: 500 μm (vertical) and 5 mm (horizontal).

the tube and are located in the exterior of the image. The pull-back image was acquired from left to right on the image, beginning from the isthmus to the fimbriated end of the tube. The OCT image revealed the isthmic part as very thin with a small muscle layer, and the outer layer of peritoneum was visible as a brighter lining on the bottom. Microvilli were compacted around the probe, creating lines that were brighter than the surrounding muscle (black arrowheads). From the isthmus, the tube transitions to the ampulla [Fig. 6(f)], represented as a conic structure that expanded the internal diameter from 2 to 4 mm. This section of the ampulla had more microvilli that were less packed in the presence of the probe, and a slight increase in muscle thickness was observed. The infundibulum shown in Fig. 6(g) had a lumen that widened into a diameter of 8 mm toward the end. In this case, the fallopian tube was manually held by the end of the infundibulum during the insertion and pullback (D_1 and D_2 represent fingers holding the tube), to preserve the fragile fimbriated end. The probe was closer to the muscle wall in this section of the pullback, explaining the apparent restriction in tube diameter. The right end of the image in Fig. 6(e) represents the fimbriated end, imaged from the internal lumen, which correlated well with the histology and external imaging results using the bench top (results not shown). Small dark inclusions (white arrows) were visible in the fimbriated end and arose from edema that leads to lymph accumulations. These structures differ from blood vessels (white star), since blood has a greater effect at attenuating the OCT signal.

4 Discussion

The imaging capabilities of OCT offer an approach for the diagnosis and detection of ovarian cancer. This paper presents a preliminary comparison of OCT images of ovarian cancer specimens with histology, and validates the potential of OCT imaging to distinguish different ovarian pathologies. This study demonstrated a good correlation between OCT images at 5× and 10× magnifications and histology sections for six types of specimens representing healthy fallopian tubes and the most frequent ovarian tumors. To capture the heterogeneity of each subclass would have required a large cohort of hundreds of patients with *ex vivo* tissue imaging to obtain the same database size as with the tissue bank. The main limitation of these comparisons was the lateral resolution (25 μm for OCT compared to 500 nm for histology), which did not allow for the assessment of fine cellular structures. Although OCT at 1300 nm cannot replace conventional pathological evaluation, it is an attractive modality to rapidly locate small benign or malignant conditions within fallopian tubes, and bridge the gap between macroscopic evaluation of the specimen as a whole and microscopic evaluation of histology slides. The various pathologies can be distinguished from one another with qualitative inspection of the OCT images throughout the acquired volumes, providing an initial assessment of the specimen before further microscopic evaluation. In addition, quantitative analysis of OCT data could potentially lead to discriminative metrics between healthy and pathological tissue requiring medical attention. Such classification can speed up the analysis of large areas (or large surface scans) of fallopian tubes, ovaries, or uterus.

The potential of OCT was extended to intraluminal imaging of freshly excised human fallopian tubes. For this purpose, we designed, assembled, and characterized a dedicated all-fiber endoscopic OCT probe and demonstrated that the measured performances of the probe agreed with the simulations and desired specifications. A minor astigmatism was measured in the air and was reduced when used in biological medium (due to the smaller refractive index mismatch between the glass capillary and the surrounding medium). When imaging surgically removed human fallopian tubes, the probe showed adequate imaging depth and multiple anatomical structures, such as the muscle layer, the mucosal layer, and the peritoneum. To our knowledge, this study yields the first OCT images of intact and freshly excised human fallopian tubes with minimal to no damage to the epithelial or subepithelial structures. It also provides the first images of the full tube, as the probe can be inserted over 10 cm in length in close contact with the mucosal layer. Imaging can be performed with minimal to no damage to the epithelial or subepithelial structures.

Notably, this probe could be adapted to *in vivo* use and screening purposes. This would require reducing the probe's external diameter and rigid length. For *in vivo* screening, the probe would have to be inserted through the uterotubal junction instead of the fimbriated end. This junction is the smallest opening of the tube with <1 mm in diameter. Flexibility is required as the tube is curved and at an angle with respect to the uterine cavity. During this study, we have noticed a variability in probe insertion easiness. Specific tubal curvature and lumen microvilli density vary for each patient. Older patients tend to have empty tubes, whereas younger patients have higher microvilli density. Navigating this convoluted structure can be difficult; a steering mechanism at the tip of the probe would help with managing the natural tubal tortuosity. In addition, the tip of the probe plays a pivotal role in the insertion process, since a poorly designed tip may be too rough on the microvilli. We found that an elliptical structure ensures a smoother insertion than a spherical shape, since it seems to displace the microvilli more gently before the passage of the probe's main body.

The design of our all-fiber endoscopic probe demonstrates promising potential as an imaging tool as it is compatible with a comprehensive imaging technology coupled with the addition of a radial scanning mechanism. This can yield a 3-D virtual fallopian tube that can be cut in any direction, under any desired/selected projection without altering the specimen. With adequate sampling, the data set of a whole fallopian tube can be represented by 20G voxels (1024 × 2000 × 10,000 voxels). Once acquired, the data could be displayed according to any transverse axis for the pathologist to review and analyze. In addition, quantitative analysis of OCT data could potentially lead to discriminative metrics between healthy and pathological tissue requiring medical attention. Such classification can speed up the analysis of large areas (or large surface scans) of fallopian tubes, ovaries, or uterus. Finally, the probe can be easily adapted to include fluorescence[24] and/or spectroscopy measurements simultaneous to the OCT imaging[32,49,51] by adding double-clad fiber to the probe and a double-clad fiber coupler to efficiently separate the signals.[51,53,54]

5 Conclusion

This paper presents, to the best of our knowledge, the first OCT images of intact human fallopian tubes. The fast acquisition rate, the in-depth imaging without altering tissue, and the volumetric image acquisition showcase OCT imaging as an efficient tool for *ex vivo* visualization of fallopian tubes and for diagnostic purposes. Notably, this imaging technique allows the scanning of a large area of the human oviducts without damaging the specimen and can be performed both on a paraffin-embedded

specimen and on fresh samples. Future work includes imaging of the inner fallopian tubes to detect benign and malignant tubal conditions in addition to comparative imaging with healthy tubes. This type of probe can also be used to image the inner cavity of the uterus through the cervix.

Disclosures

Acknowledgments

References

1. G. C. E. Stuart et al., "2010 Gynecologic Cancer InterGroup (GCIG) consensus statement on clinical trials in ovarian cancer," *Int. J. Gynecol. Cancer* **21**(4), 750–755 (2011).
2. I. J. Jacobs et al., "Ovarian cancer screening and mortality in the UK collaborative trial of ovarian cancer screening (UKCTOCS): a randomised controlled trial," *Lancet* **387**(10022), 945–956 (2016).
3. S. H. George, R. Garcia, and B. M. Slomovitz, "Ovarian cancer: the fallopian tube as the site of origin and opportunities for prevention," *Front. Oncol.* **6**, 108 (2016).
4. A. N. Karnezis et al., "The disparate origins of ovarian cancers: pathogenesis and prevention strategies," *Nat. Rev. Cancer Perspect.* **17**(1), 65–74 (2017).
5. C. Corzo et al., "Role of fallopian tubes in the development of ovarian cancer," *J. Minimally Invasive Gynecol.* **24**(2), 230–234 (2017).
6. V. A. Moyer, on behalf of the U.S. Preventive Services Task Force, "Screening for ovarian cancer: U.S. preventive services task force reaffirmation recommendation statement," *Ann. Intern. Med.* **157**(12), 900–904 (2012).
7. B. Rosen et al., "The impacts of neoadjuvant chemotherapy and of debulking surgery on survival from advanced ovarian cancer," *Gynecol. Oncol.* **134**(3), 462–467 (2014).
8. I. Vergote et al., "Neoadjuvant chemotherapy or primary surgery in stage IIIC or IV ovarian cancer," *N. Engl. J. Med.* **363**(10), 943–953 (2010).
9. R. I. Olivier et al., "Clinical outcome of prophylactic oophorectomy in BRCA1/BRCA2 mutation carriers and events during follow-up," *Br. J. Cancer* **90**(8), 1492–1497 (2004).
10. A. P. M. Finch et al., "Impact of oophorectomy on cancer incidence and mortality in women with a BRCA1 or BRCA2 mutation," *J. Clin. Oncol.* **32**(15), 1547–1553 (2014).
11. S. Kyriazi, S. B. Kaye, and N. M. deSouza, "Imaging ovarian cancer and peritoneal metastases–current and emerging techniques," *Nat. Rev. Clin. Oncol.* **7**(7), 381–393 (2010).
12. D. A. Bell, "Origins and molecular pathology of ovarian cancer," *Mod. Pathol.* **18**, S19–S32 (2005).
13. R. J. Kurman and I. M. Shih, "The origin and pathogenesis of epithelial ovarian cancer—a proposed unifying theory," *Am. J. Surg. Pathol.* **34**(3), 433–443 (2010).
14. H. Makhlouf et al., "Multispectral confocal microendoscope for in vivo and in situ imaging," *J. Biomed. Opt.* **13**(4), 044016 (2008).
15. S. Srivastava et al., "Computer-aided identification of ovarian cancer in confocal microendoscope images," *J. Biomed. Opt.* **13**(2), 024021 (2008).
16. A. A. Tanbakuchi et al., "In vivo imaging of ovarian tissue using a novel confocal microlaparoscope," *Am. J. Obstet. Gynecol.* **202**(1), e1–e9 (2010).
17. T.-Y. Wu et al., "Confocal microlaparoscope for imaging the fallopian tube," *J. Biomed. Opt.* **19**(11), 116010 (2014).
18. N. D. Kirkpatrick, M. A. Brewer, and U. Utzinger, "Endogenous optical biomarkers of ovarian cancer evaluated with multiphoton microscopy," *Cancer Epidemiol. Biomarkers Prev.* **16**(10), 2048–2057 (2007).
19. O. Nadiarnykh et al., "Alterations of the extracellular matrix in ovarian cancer studied by second harmonic generation imaging microscopy," *BMC Cancer* **10**, 94–94 (2010).
20. G. M. van Dam et al., "Intraoperative tumor-specific fluorescence imaging in ovarian cancer by folate receptor-α targeting: first in-human results," *Nat. Med.* **17**(10), 1315–1319 (2011).
21. T. E. Renkoski, K. D. Hatch, and U. Utzinger, "Wide-field spectral imaging of human ovary autofluorescence and oncologic diagnosis via previously collected probe data," *J. Biomed. Opt.* **17**(3), 036003 (2012).
22. S. D. Kamath et al., "Autofluorescence of normal, benign, and malignant ovarian tissues: a pilot study," *Photomed. Laser Surg.* **27**(2), 325–335 (2009).
23. R. George et al., "Parallel factor analysis of ovarian autofluorescence as a cancer diagnostic," *Lasers Surg. Med.* **44**(4), 282–295 (2012).
24. J. N. McAlpine et al., "Autofluorescence imaging can identify preinvasive or clinically occult lesions in fallopian tube epithelium: a promising step towards screening and early detection," *Gynecol. Oncol.* **120**(3), 385–392 (2011).
25. T. H. Tate et al., "Multispectral fluorescence imaging of human ovarian and fallopian tube tissue for early-stage cancer detection," *J. Biomed. Opt.* **21**(5), 056005 (2016).
26. C. M. Krishna et al., "Evaluation of the suitability of ex vivo handled ovarian tissues for optical diagnosis by Raman microspectroscopy," *Biopolymers* **79**(5), 269–276 (2005).
27. K. Maheedhar et al., "No diagnosis of ovarian cancer by Raman spectroscopy: a pilot study," *Photomed. Laser Surg.* **26**(2), 83–90 (2008).
28. D. Huang et al., "Optical coherence tomography," *Science* **254**(5035), 1178–1181 (1991).
29. Y. Yasuno, V. D. Madjarova, and S. Makita, "Three-dimensional and high-speed swept-source optical coherence tomography for in vivo investigation of human anterior eye segments," *Opt. Express* **13**(26), 10652–10664 (2005).
30. T. Wang et al., "Heartbeat OCT: in vivo intravascular megahertz-optical coherence tomography," *Biomed. Opt. Express* **6**(12), 5021–5032 (2015).
31. L. H. Simmons et al., "Su1717 screening for Upper GI disease in the primary care office with tethered capsule OCT endomicroscopy," *Gastrointest. Endoscopy* **81**(5), AB389–AB390 (2016).
32. H. Yoo et al., "Intra-arterial catheter for simultaneous microstructural and molecular imaging in vivo," *Nat. Med.* **17**(12), 1680–1684 (2011).
33. S. Huang et al., "In vivo imaging of retinal hemodynamics with OCT angiography and Doppler OCT," *Biomed. Opt. Express* **7**(2), 663–663 (2016).
34. I. Gorczynska et al., "Comparison of amplitude-decorrelation, speckle-variance and phase-variance OCT angiography methods for imaging the human retina and choroid," *Biomed. Opt. Express* **7**(3), 911–942 (2016).
35. E. Shieh et al., "Diagnostic performance of a novel 3D neuroretinal rim parameter for glaucoma using high-density volume scans," *Am. J. Ophthalmol.* **169**, 168–178 (2016).
36. M. J. Suter et al., "Comprehensive microscopy of the esophagus in human patients with optical frequency domain imaging," *Gastrointest. Endoscopy* **68**(4), 745–753 (2008).
37. G. J. Ughi et al., "Automated segmentation and characterization of esophageal wall in vivo by tethered capsule optical coherence tomography endomicroscopy," *Biomed. Opt. Express* **7**(2), 409–419 (2016).
38. G. J. Tearney et al., "Consensus standards for acquisition, measurement, and reporting of intravascular optical coherence tomography studies: a report from the International Working Group for intravascular optical coherence tomography standardization and validation," *J. Am. Coll. Cardiol.* **59**(12), 1058–1072 (2012).

39. G. J. Ughi et al., "Clinical characterization of coronary atherosclerosis with dual-modality OCT and Near-infrared autofluorescence imaging," *JACC: Cardiovasc. Imaging* **9**(11), 1304–1314 (2016).

40. C. Pitris et al., "High resolution imaging of gynecologic neoplasms using optical coherence tomography," *Obstet. Gynecol.* **93**(1), 135–139 (1999).

41. M. Ascencio et al., "The role and value of optical coherence tomography in gynecology," *J. Gynecol. Obstet. Biol. Reprod.* **36**(8), 749–755 (2007).

42. A. Sergeev et al., "In vivo endoscopic OCT imaging of precancer and cancer states of human mucosa," *Opt. Express* **1**(13), 432–440 (1997).

43. J. M. Herrmann et al., "Two- and three-dimensional high-resolution imaging of the human oviduct with optical coherence tomography," *Fertil. Steril.* **70**(1), 155–158 (1998).

44. J. L. Fine et al., "Direct scanning of pathology specimens using spectral domain optical coherence tomography: a pilot study," *Ophthalmic Surg. Lasers Imaging* **41**(6), 1–13 (2011).

45. M. Kirillin et al., "Criteria for pathology recognition in optical coherence tomography of fallopian tubes," *J. Biomed. Opt.* **17**(8), 081413 (2012).

46. L. P. Hariri et al., "Laparoscopic optical coherence tomography imaging of human ovarian cancer," *Gynecol. Oncol.* **114**(2), 188–194 (2009).

47. M. A. Brewer et al., "Imaging of the ovary," *Technol. Cancer Res. Treat.* **3**(6), 617–627 (2004).

48. M. Keenan et al., "Design and characterization of a combined OCT and wide field imaging falloposcope for ovarian cancer detection," *Biomed. Opt. Express* **8**(1), 124–136 (2017).

49. H. Pahlevaninezhad et al., "Endoscopic high-resolution autofluorescence imaging and OCT of pulmonary vascular networks," *Opt. Lett.* **41**(14), 3209–3212 (2016).

50. Y. Mao et al., "Graded-index fiber lens proposed for ultrasmall probes used in biomedical imaging," *Appl. Opt.* **46**(23), 5887–5894 (2007).

51. L. Scolaro et al., "Molecular imaging needles: dual-modality optical coherence tomography and fluorescence imaging of labeled antibodies deep in tissue," *Biomed. Opt. Express* **6**(5), 1767–1781 (2015).

52. W.-J. Madore et al., "Morphologic 3D scanning of fallopian tubes to assist ovarian cancer diagnosis," *Proc. SPIE* **9689**, 96894D (2016).

53. W.-J. Madore et al., "Asymmetric double-clad fiber couplers for endoscopy," *Opt. Lett.* **38**(21), 4514–4517 (2013).

54. H. Pahlevaninezhad et al., "A high-efficiency fiber-based imaging system for co-registered autofluorescence and optical coherence tomography," *Biomed. Opt. Express* **5**(9), 2978–2987 (2014).

Biographies for the authors are not available.